frontiers
in Energy Research

ORIGINAL RESEARCH
published: 27 May 2021
doi: 10.3389/fenrg.2021.682008

Assessing the Electrochemical Stability Window of NASICON-Type Solid Electrolytes

*Yasmine Benabed[1,2], Maxime Rioux[1], Steeve Rousselot[1], Geoffroy Hautier[2,3] and Mickaël Dollé[1]**

[1]Laboratory of Chemistry and Electrochemistry of Solids, Department of Chemistry, Université de Montréal, Montréal, QC, Canada, [2]Institute of Condensed Matter and Nanosciences, Université Catholique de Louvain, Louvain-la-Neuve, Belgium, [3]Thayer School of Engineering, Dartmouth College, Hanover, NH, United States

All-Solid-State Lithium Batteries (ASSLBs) are promising since they may enable the use of high potential materials as positive electrode and lithium metal as negative electrode. This is only possible through solid electrolytes (SEs) stated large electrochemical stability window (ESW). Nevertheless, reported values for these ESWs are very divergent in the literature. Establishing a robust procedure to accurately determine SEs' ESWs has therefore become crucial. Our work focuses on bringing together theoretical results and an original experimental set up to assess the electrochemical stability window of the two NASICON-type SEs $Li_{1.3}Al_{0.3}Ti_{1.7}(PO_4)_3$ (LATP) and $Li_{1.5}Al_{0.5}Ge_{1.5}(PO_4)_3$ (LAGP). Using first principles, we computed thermodynamic ESWs for LATP and LAGP and their decomposition products upon redox potentials. The experimental set-up consists of a sintered stack of a thin SE layer and a SE-Au composite electrode to allow a large contact surface between SE and conductive gold particles, which maximizes the redox currents. Using Potentiostatic Intermittent Titration Technique (PITT) measurements, we were able to accurately determine the ESW of LATP and LAGP solid electrolytes. They are found to be [2.65–4.6 V] and [1.85–4.9 V] for LATP and LAGP respectively. Finally, we attempted to characterize the decomposition products of both materials upon oxidation. The use of an O_2 sensor coupled to the electrochemical setup enabled us to observe *operando* the production of O_2 upon LAGP and LATP oxidations, in agreement with first-principles calculations. Transmission Electron Microscopy (TEM) allowed to observe the presence of an amorphous phase at the interface between the gold particles and LAGP after oxidation. Electrochemical Impedance Spectroscopy (EIS) measurements confirmed that the resulting phase increased the total resistance of LAGP. This work aims at providing a method for an accurate determination of ESWs, considered a key parameter to a successful material selection for ASSLBs.

Keywords: electrochemical stability window, potentiostatic intermittent titration technique, spark plasma sintering, solid electolyte, all-solid-state lithium batteries, grand potential phase diagram, NASICON

Edited by:
Chi Chen,
University of California, San Diego,
United States

Reviewed by:
Weike Ye,
University of California, San Diego,
United States
Xingyu Guo,
University of California, San Diego,
United States
Liqiang Mai,
Wuhan University of Technology,
China

***Correspondence:**
Mickaël Dollé
mickael.dolle@umontreal.ca

Specialty section:
This article was submitted to Electrochemical Energy Conversion and Storage,
a section of the journal Frontiers in Energy Research

Received: *17 March 2021*
Accepted: *03 May 2021*
Published: *27 May 2021*

Citation:
Benabed Y, Rioux M, Rousselot S, Hautier G and Dollé M (2021) Assessing the Electrochemical Stability Window of NASICON-Type Solid Electrolytes. Front. Energy Res. 9:682008. doi: 10.3389/fenrg.2021.682008

INTRODUCTION

Since their commercialization in 1990, rechargeable lithium-ion batteries (LIBs) have revolutionized global communication and enabled the democratization of portable electronics. LIBs have grown to become a well-established, efficient energy-storage technology in terms of power density and life span. However, commercialized LIBs contain highly flammable and toxic organic liquids as electrolyte ($LiPF_6$ in carbonate-based solvents), entailing significant safety hazard. Moreover, currently used liquid electrolytes hinder the use of lithium metal as a negative electrode material and the commercialization of high-energy-density Li-metal battery systems (Aurbach et al., 2002; Lin et al., 2017). Lithium metal displays a remarkably high theoretical capacity and is considered the best negative electrode material for lithium batteries (3,860 mA $h.g^{-1}$, −3.05 V vs. SHE) (Winter and Besenhard, 1999). Nevertheless, lithium metal batteries fail to achieve commercialization with conventional carbonate-based liquid electrolytes because of lithium metal's low cycling efficiency and its detrimental formation of lithium dendrites (Orsini et al., 1998). Upon cycling, the growth of dendrites at the surface of Li-metal electrodes can lead to short-circuits and thermal runaways. Moreover, the limited electrochemical stability window (ESW) of organic liquid electrolytes (up to 4.2 V vs. Li^+/Li) limits the choice of positive electrode materials in LIBs. High potential positive electrode materials, such as $LiNi_{0.5}Mn_{1.5}O_4$, $LiNi_{0.8}Co_{0.15}Al_{0.05}O_2$ and $LiNi_xMn_yCo_zO_2$ (Thackeray et al., 1983; Li, 1997; Liu et al., 1999; Yoshio et al., 2000), require the use of an electrolyte stable in the range of their operation potentials. To tackle these problems, researchers have been working toward developing a new generation of high-power lithium batteries, namely all-solid-state lithium batteries (ASSLBs).

ASSLBs are sparking rising interest thanks to their enhanced safety, achieved by replacing the flammable and reactive conventional liquid electrolyte with a safer and more thermally stable ceramic or polymer solid-state electrolyte (SE) (Gao et al., 2018; Zhang et al., 2018; Zheng et al., 2018; Bag and Thangadurai, 2020). Several families of ceramic SEs have been investigated based on their ionic conductivity as well as thermal and chemical stability. Sulfur-based SE such as $Li_{10}GeP_2S_{12}$ from the thio-LiSICON family (derived from β-Li_3PO_4 crystal structure) and Argyrodites (products of the Li_2S-P_2S_5-LiX phase diagram with X = Cl, Br, I), display very promising conductivities (up to 10^{-2} $S.cm^{-1}$ at room temperature (Kamaya et al., 2011)) but suffer from severe chemical instability/sensitivity to air or moisture, causing the generation of toxic H_2S gas (Muramatsu et al., 2011; Weber et al., 2016). Studies have also demonstrated the thermal and electrochemical instability of sulfide-based SE, leading to harmful battery degradation and safety issues (Sakuda et al., 2010; Muramatsu et al., 2011; Auvergniot et al., 2017; Chen et al., 2018; Zhang et al., 2018; Zhang et al., 2019). Oxide-based SE families, such as NASICONs ($Na_{1+x}Zr_2P_{3-x}Si_xO_{12}$), garnets ($A_3B_2X_3O_{12}$) and perovskites ($ABO_3$) display good conductivities ($10^{-3/-4}$ $S.cm^{-1}$ at room temperature) and have the advantage over sulfides to be less air and moisture-sensitive, leading to much easier handling despite requiring higher sintering temperatures (Meesala et al., 2017; Lau et al., 2018; Zheng et al., 2018). Therefore, oxide-based ceramics appear to be the most practical and reliable type of SE developed to date. NASICON-type SEs such as $Li_{1.5}Al_{0.5}Ge_{1.5}(PO_4)_3$ (LAGP) and $Li_{1.3}Al_{0.3}Ti_{1.7}(PO_4)_3$ (LATP) were particularly investigated for their ionic conductivities up to 1.09×10^{-3} $S.cm^{-1}$ and 5.08×10^{-3} $S.cm^{-1}$ at room temperature respectively (Thokchom and Kumar, 2008; Hupfer et al., 2016) and their stability against water and air (Imanishi et al., 2008; Hasegawa et al., 2009). ASSLBs are developed with the prospect of using lithium metal as negative electrode and high potential materials as positive electrode to significantly increase LIBs power and energy densities. ASSLBs can only meet these expectations because of the SEs presumed large electrochemical stability windows. However, assessing ESWs relies strongly on the type of characterization technique and experimental settings. Therefore, values for these electrochemical windows are very divergent in the literature published through the last decade. For example, as shown in **Table 1**, reported values for the ESWs of LAGP and LATP depend on the electrochemical technique used. Recently, several studies have come to specifically decry the frequent overestimation of solid electrolytes ESWs (Han et al., 2016; Tian et al., 2017; Zhang et al., 2018; Schwietert et al., 2020), which are proven to be much more limited in practice (Cui et al., 2016; Han et al., 2016; Wenzel et al., 2016; Chung and Kang, 2017). To characterize the ESW using cyclic voltammetry (CV), ceramic solid electrolytes are pressed into pellets and coated with a conductive metal (Au) before placing them between an inert blocking electrode (stainless steel, Pt or Au) and a polymer protected lithium metal electrode for cycling. In this configuration, a very limited contact area is available between the SE and the inert blocking electrode. Being in a solid-state medium, only the portion of SE in contact with the coated metal is expected to react. If the reaction forms a solid insulating phase, only the first few nanometers of the SE will react at the SE-Au coating interface as electrons cannot reach the reaction front. Resulting redox currents are therefore relatively small and hardly noticeable on CV curves. Moreover, using high sweeping speeds and omitting the ohmic drop correction can also alter the CV curve (Bard and Faulkner, 2000). Tested through this method,

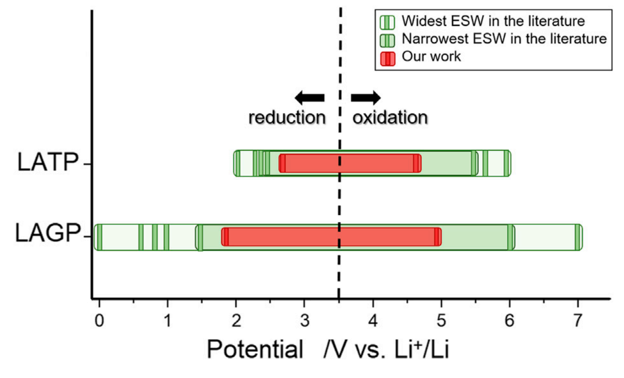

GRAPHICAL ABSTRACT | Electrochemical stability windows for $Li_{1.3}Al_{0.3}Ti_{1.7}(PO_4)_3$ (LATP) and $Li_{1.5}Al_{0.5}Ge_{1.5}(PO_4)_3$ (LAGP) reported in the literature.

TABLE 1 | Electrochemical stability windows for LAGP and LATP SEs reported in the literature.

SE	E_{red}/V	E_{ox}/V	Technique used	Cell config.	Scan rate	Year	References
LAGP	0	>6	CV	Au@LAGP@Au	0.5 mV/s	2007	Xu et al. (2007)
	0.85	7	CV	Ag@LAGP|Li	0.1 mV/s	2010	Feng et al. (2010)
	0.6	>6	CV	$LiMn_2O_4$|LAGP|Li	0.1 mV/s	2013	Feng et al. (2013)
	1	>6	CV	Au@LAGP|Li	0.5 mV/s	2017	Zhang et al. (2017)
	1.5		CV	Au@TiO_2|LAGP|Li	1 mV/s	2011	Kotobuki et al. (2011)
LATP	2.3	6	Galvanostatic	Li_2S|LATP|Li	nd	2019	Xiao et al. (2019)
	2.45		Galvanostatic	Li|LATP|Li	nd	2020	Zhu et al. (2020)
	2.4		CV	Liquid config	0.5 mV/s	2006	Xu et al. (2006)
	2.4		Coulombic titration	Mo@LATP|Li	nd	1999	Birke et al. (1999)
	<2	5.67[a]	LSV	Liquid config	10 mV/s	2018	Shi et al. (2018)
		5.5[a]	LSV	$LiMn_2O_4$|LATP|Li	0.1 mV/s	2018	Liang et al. (2018)

[a] *These values are reported for PVDF/LATP composites but are attributed to the contribution of LATP.*

very wide ESWs can be reported. However, solid electrolytes including LAGP, LATP, $Li_{0.35}La_{0.55}TiO_3$ (LLTO), and $Li_{3.5}Zn_{0.25}GeO_4$ (LiSICON) were investigated through alternative techniques, such as *in situ* X-ray Photoelectron Spectroscopy (XPS) and Energy-Dispersive X-ray Spectroscopy (EDS), the results revealed much higher reduction potentials than previously established by CV (Alpen et al., 1978; Knauth, 2009; Hartmann et al., 2013; Wenzel et al., 2015). Based on first-principles studies, most ESWs appear much narrower than expected experimentally (Ong et al., 2013; Zhu et al., 2015; Richards et al., 2016; Zhu et al., 2016). Zhu et al. (2015) suggest that the practical stability of SE materials is not thermodynamically intrinsic but is rather due to kinetic phase stabilizations. The sluggish kinetics of the decomposition reactions happening at the extremes of the ESWs cause a high overpotential, leading to wider experimental electrochemical windows. To justify this difference, Schwietert et al. (2020) suggested that the favourable decomposition pathway for some SE was indirect rather than direct, *via* (de)lithiated states of the solid electrolyte, into the thermodynamically stable decomposition products.

In this study, we intend to establish a robust way to efficiently assess ESWs for the two NASICON-type materials $Li_{1+x}Al_xM_{2-x}(PO_4)_3$ (M = Ge, Ti). Using first principles, we computed thermodynamic ESWs for LATP and LAGP and predicted their decomposition products upon redox potentials to gain more insight on the decomposition mechanisms. Experimentally, spark plasma sintering (SPS) technology was used to sinter together active material (SE) and conductive metal (Au) into a composite electrode to maximize the contact area between them and therefore increase the decomposition currents. Using Au as the conductive metal instead of commonly used carbon black prevent any side/decomposition reaction during sintering. Additionally, carbon black has the disadvantage to absorb a significant amount of moisture despite extensive drying (Plummer, 1930; Dewey et al., 1932; Liu et al., 2017), resulting in electrochemical artifacts above 4 V vs. Li^+/Li. Gold is inert and stable through a large electrochemical window (Vetter and Berndt, 1958; Jiang et al., 2010) and allows an excellent electronic conductivity. Potentiostatic intermittent titration technique (PITT) was used instead of CV to ensure a constant return to equilibrium and allow locating the redox potentials with great precision. The technique is coupled with an O_2 sensing probe in order to observe the production of O_2 from the materials' decomposition. Transmission electron microscopy (TEM) and electrochemical impedance spectroscopy (EIS) measurements were carried out to gain more insight on the oxidation process of LAGP. The collected results challenge the claimed electrochemical stability windows of LAGP and LATP materials measured until now. This paper provides a more accurate determination of the ESW for solid electrolytes and should allow a more thought-through material selection of SEs for ASSLBs.

MATERIALS AND METHODS

Grand Potential Phase Diagram (GPPD)

The GPPD is used to compute the ESWs of LAGP and LATP. The GPPD is constructed from a phase diagram by keeping the system open to Li. To construct such phase diagrams, the relevant free energy is the grand potential Φ, it is determined for each composition **c** at a given chemical potential $\mu_{\mathbf{Li}}$. The grand potential is derived from the Legendre transform of the energy (Ong et al., 2008), following the equation:

$$\Phi_{(c,\mu_{Li})} = E_{(c)} - n_{Li}(c)\mu_{Li} \tag{1}$$

Where $E_{(c)}$ is the energy of composition c, $n_{Li}(c)$ is the number of lithium atoms found in the composition c and μ_{Li} is the chemical potential of lithium. The GPPD is constructed from the grand potentials of all relevant compositions at 0 K and incorporates all the stable phases of the initial phase diagram. The electrochemical stability window of a SE is the range of potentials over which the SE phase is considered stable. When using the GPPD, the ESW is the range of chemical potentials μ_{Li} over which the SE composition is considered stable (energy above Hull = 0) relatively to competing compositions of the phase diagram. The conversion from chemical potential to potential vs. Li^+/Li is achieved following the equation:

$$V = -\frac{\mu_{Li} - \mu^{o}_{Li}}{e} \tag{2}$$

Where μ_{Li} is the standard computed energy for lithium metal, **e** is the elementary electron charge. Decomposition products for the SEs are identified to be the most stable compositions (energy above Hull = 0) in which the SE decomposes, at the ESW limits.

All relevant compositions and their computed enthalpies are collected from The Materials Project database (Jain et al., 2013). The GPPD is generated for LAGP and LATP phase diagrams over a [0–8.0] V vs. Li^+/Li potential range, using Pymatgen software package (Ong et al., 2013). Compositions' energies were computed with DFT within the projector augmented wave (PAW) formalism (Blöchl, 1994), using the Pedrew-Burke-Ernzerhof (PBE) generalized gradient approximation (GGA) to the exchange-correlation energy (Perdew et al., 1996), implemented in the Vienna ab initio simulation package (VASP) (Kresse and Furthmüller, 1996). Calculation parameters include a cutoff energy of 520 eV and a k-point grid of $500/n_{atoms}$.

Reactants Syntheses

LAGP ceramic was synthesized using $LiOH{\cdot}H_2O$ (Nemaska Lithium), $Al(OH)_3$ (Alfa Aesar), GeO_2 (Strem) and $(NH_4)_2HPO_4$ (Sigma Aldrich) in stoichiometric ratios. The starting materials were ground manually for 10 min in a porcelain mortar and heated in a Pyrex beaker at 400°C (2°C/min heating rate) for 18 h to allow complete phosphating and gradually remove all decomposition gases (i.e. NH_3, H_2O). The powder was melted at 1,200°C inside a fused silica crucible for 1 h and the resulting liquid was casted into a stainless-steel mold at room temperature. The resulting colorless glass was ground into a fine powder during 20 min in a zirconia high energy ball mill (SPEX 8,000M Mixer Mill). To obtain the LAGP ceramic, the glass powder was annealed at 580°C in a fused silica crucible for 48 h, between the glass transition (T_g = 520°C) and crystallization (T_c = 610°C) temperatures (Fu, 1997), allowing complete crystallization of the glass. All the heating steps were performed in an electric furnace. LATP was synthesized by dissolving stoichiometric amounts of $NH_4H_2PO_4$ and TiO_2 (Sigma Aldrich) in deionized water (Holzapfel et al., 2012). The resulting solution was stirred continuously and heated under reflux at 160°C for 16 h. After cooling down to 80°C, $Al(OH)_3$ was added to the solution and stirred for 30 min. Dissolved $LiOH{\cdot}H_2O$ in deionized water was added at last before drying the final mixture at 300°C overnight. The resulting powder was milled using a zirconia high energy ball mill (SPEX 8,000M Mixer Mill) for 30 min. Finally, the powder was loaded in a crucible and annealed at 900°C for 6 h (2°C/min heating rate).

Spark Plasma Sintering

SPS experiments were carried out to sinter SE-Au/SE stacks using a Dr Sinter Lab Jr series 632Lx SPS. Au powder (Sigma Aldrich, CAS number 265772, <45 μm, 99.99% trace metals basis) and SE ceramic powder (LAGP or LATP) were mixed in an agate mortar following a 25:75 wt% ratio of SE:Au (2:1 v%). Au is introduced in large quantities to make up for its high density and allow a large surface area of contact with LAGP or LATP. 150 mg of the resulting powder were loaded into a Grafoil® coated graphite die (Ø = 8 mm) and pressed between two graphite punches. The Grafoil® is used to favor the demolding. The graphite die was placed inside the SPS chamber between two graphite spacers and uniaxially pressed at 100 MPa for 15 min to maximize particle cohesion. 75 mg of the SE powder were homogenously spread on top of the pre-compressed SE-Au pellet. The graphite die was placed inside the SPS chamber a second time and pressed at 100 MPa under vacuum. The sintering was performed up to 650°C for LAGP-Au/LAGP and 850°C for LATP-Au/LATP at a 50°C/min heating rate, where it was kept for 3–5 min before cooling down to room temperature at a 100°C/min rate. Voltage and current used in the process were applied under automatic operation mode. The resulting SE-Au/SE stacks were then placed in an electric furnace and heated to 750°C at a 5°C/min rate, under air for 18 h, to gradually calcinate and remove the remaining Grafoil® off the pellets. The pellets were then manually polished using Buehler® silicon carbide papers of different grain sizes (280, 400, and 1,000 grits) followed by diamond polishing paper to reach a final surface finish of 1 μm.

Specific Surface Area

The specific surface area of the gold particles was determined by the Brunauer-Emmett-Teller (BET) theory using a Micromeritics Gemini V. Prior to measurements, 500 mg of gold were degassed for 1 h at 200°C under N_2 gas to remove water.

Powder X-Ray Diffraction (PXRD)

PXRD measurements were carried out on pellets using a Panalytical Empyrean diffractometer with copper X-ray sealed tube (CuKα, operated at 45 kV/40 mA, automatic optics iCore and dCore, reflection transmission spinner and a hybrid pixel detector PIXcel 3D). PXRD measurements were collected at a 0.4°/min rate from 10 to 80° in 2θ.

Scanning Electron Microscopy (SEM)

Analyses of the stacks were carried out on an Oxford Instrument JEOL JSM-7600TFE microscope equipped with a field emission gun (FEG). Samples were mounted in epoxy resin, polished with Buehler® silicon carbide papers of different grain sizes (280, 400, and 1,000 grits) followed by diamond polishing paper to reach a final surface finish of 1 μm. The samples were then sputtered with chromium (10 nm). Views were taken with zooms ranging from ×30 to ×10k. SEM analyses were coupled to energy-dispersive X-ray spectroscopy (EDS) measurements using an Oxford Instruments X-Max N 80 with an 80 mm^2 silicon drift detector (SDD).

Electrochemical Measurements

The SE-Au/SE stacks were tested in electrochemistry using two-electrode stainless steel Swagelok cells. All the stacks and Swagelok parts were thoroughly dried at 140°C before mounting them inside an argon-filled glovebox (4 ppm O_2 and 0.1 ppm H_2O). SE-Au/SE stacks acted as working electrode and electrolyte. A lithium metal electrode protected with a thin layer of polyethylene oxide (PEO) polymer-based electrolyte was placed against the SE part of the stack. A protective teflon ring was introduced to impede the PEO or Li metal from coming in contact with the positive electrode in case of POE creeping. PEO electrolyte was prepared by mixing PEO (5M, Sigma Aldrich) with Lithium Bis(trifluoromethylsulfonyl)amine (Solvionics) using a [EO]:[Li] ratio of 20:1 in a closed internal mixer Brabender®

TABLE 2 | Computed electrochemical stability windows for LAGP and LATP using the GPPD and their computed decomposition products.

SE	E_{RED}/V	Decomposition products	E_{OX}/V	Decomposition products	References
LAGP	2.72	GeO_2, Ge, $Li_4P_2O_7$, $AlPO_4$	4.29	O_2, $Ge_5O(PO_4)_6$, $AlPO_4$, $LiPO_3$	This work
	2.70	GeO_2, Ge, $Li_4P_2O_7$, $AlPO_4$	4.27	O_2, $Ge_5O(PO_4)_6$, $AlPO_4$, $Li_4P_2O_7$	Zhu et al. (2015)
LGP	2.72		4.30		This work
	2.95	GeO_2, Ge, $LiPO_3$	4.40	O_2, GeO_2, GeP_2O_7	Richards et al. (2016)
LATP	2.19	$AlPO_4$, $Li_2Ti_2(PO_4)_3$	4.67	O_2, $AlPO_4$, TiP_2O_7, $Ti_5(PO_5)_4$	This work
	2.16	$AlPO_4$, P, $LiTiPO_5$, Li_3PO_4	4.31	O_2, $AlPO_4$, $LiTi_2(PO_4)_3$, $Li_4P_2O_7$	Zhu et al. (2015)
LTP	2.17		4.65		This work
	2.70	$Li_2Ti_2(PO_4)_3$	4.75	$Ti_5P_6O_{25}$, TiP_2O_7, Ti_2O_7	Richards et al. (2016)
	2.37		4.59		Xiao et al. (2019)

(30 ml volume of the working chamber) at 170 ± 5°C. The blend is then laminated between steel plates. The polymer synthesis was carried out in an argon-filled glovebox to minimize exposure to air and water (Foran et al., 2020; Mankovsky et al., 2020). The electrochemical tests were performed at 60°C on a VMP2 series multichannel potentiostat (Bio-Logic Science Instruments). The ESWs were measured using PITT, small voltage increments of 50 mV were applied to cycle the stacks from E_{oc} down to 0 V vs. Li^+/Li for reduction and up to 6 V vs. Li^+/Li for oxidation. The next 50 mV increment was applied each time the current dropped below 10 nA or after a relaxation time of 3 h. When coupled to the O_2 sensing probe, an accelerated version of the PITT was used instead; voltage increments of 100 mV were applied after the current dropped below 10 nA or after a relaxation time of 1 h. EIS measurements were carried out on Au-coated LAGP pellets, at frequencies ranging from 200 kHz to 2 mHz with an amplitude of 10 mV, from E_{oc} to 5.6 V. Prior to EIS measurements, each potential step was stabilized for 3 h, similarly to PITT settings. EC-Lab® software was used to analyze the data.

O_2 Sensing

Oxygen sensing measurements were performed using a southland sensing OMD-501D oxygen sensor. The setup combines O_2 sensing and accelerated PITT cycling on SE-Au/SE stacks for an *operando* measure of O_2. The O_2 sensor was assembled using a T-Swagelok cell under argon. The electrochemical cells were left at open-circuit potential for at least 6 h prior to cycling in order to establish an O_2 baseline.

Transmission Electron Microscopy

Milling of samples by FIB was performed using an Hitachi FB 2000A focused ion beam (FIB) system operating at 30 keV with a 50–100 nm resolution. An intense beam of Ga ions is produced using a high-brightness liquid–metal ion source and a double lens focusing system. A gun to deposit tungsten was used to cover and protect areas selected for characterization. An *in situ* lift-out FIB technique was used to prepare TEM samples, it was used to extract a thin lamella, which was then fixed to a Cu half-disk TEM support using tungsten deposition and welding. TEM observations were carried out using an Oxford Instruments JEOL JEM 2100F FEG-TEM microscope, operated at 200 kV. Image acquisition was done on bright field mode.

RESULTS AND DISCUSSION

Grand Potential Phase Diagram

Table 2 shows the ESWs for LAGP and LATP computed in this study and compare them to other values found in the literature. LAGP was found stable between 2.72 and 4.29 V vs. Li^+/Li, LATP between 2.19 and 4.67 V vs. Li^+/Li. Zhu et al. (2016) also computed LATP and LAGP electrochemical stability windows, they are presented in **Table 2**, and are in good agreement with our results. Other similar values were found in the literature for non-doped NASICON $LiGe_2(PO_4)_3$ and $LiTi_2(PO_4)_3$ which compare fairly with our results of [2.72–4.30 V] for $LiGe_2(PO_4)_3$ and [2.17–4.65 V] for $LiTi_2(PO_4)_3$. Computed results are coherent with one another, it proves that GPPD is a robust and appropriate method to use to compute ESWs. It was possible to derive from the GPPD the decomposition products for LATP and LAGP upon oxidation and reduction. Regarding LAGP, the decomposition products are found to be GeO_2, Ge, $Li_4P_2O_7$, and $AlPO_4$ for reduction and are in perfect agreement with the computed results of Zhu et al. and the experimental results from Sun et al. (2020) (Paolella et al., 2020). Similarly, O_2, $Ge_5O(PO_4)_6$, and $AlPO_4$ as the decomposition products of LAGP upon oxidation are recurrent in our study and for Zhu *et al.* Regarding LATP, the decomposition product upon reduction are $AlPO_4$ and $Li_2Ti_2(PO_4)_3$. $AlPO_4$ is found in our work and for Zhu *et al.* Our computations also predict the production of $Li_2Ti_2(PO_4)_3$, indicating a possible insertion of lithium in LATP at low potential. Upon oxidation, the decomposition products are found to be O_2, $AlPO_4$, TiP_2O_7, and $Ti_5(PO_5)_4$. The production of O_2 and $AlPO_4$ was also predicted by Zhu *et al.* The computed values for thermodynamic ESW are expected to differ from the experimental values due to the kinetic contribution but guide us in the coming experimental part. In the same manner, the computed decomposition products for oxidation, especially $AlPO_4$ and O_2, give a valuable insight of the degradation mechanism of LAGP and LATP and guide us in characterizing the decomposition products experimentally.

Synthesis and Sintering of SE-Au/SE Stacks

Prior to any electrochemical measurement, it is essential to validate the quality of the stack preparation both from a chemical and a mechanical point of view. Unexpected reactions between SE and gold particles are likely to occur during the sintering at high temperature (Delaizir et al., 2012).

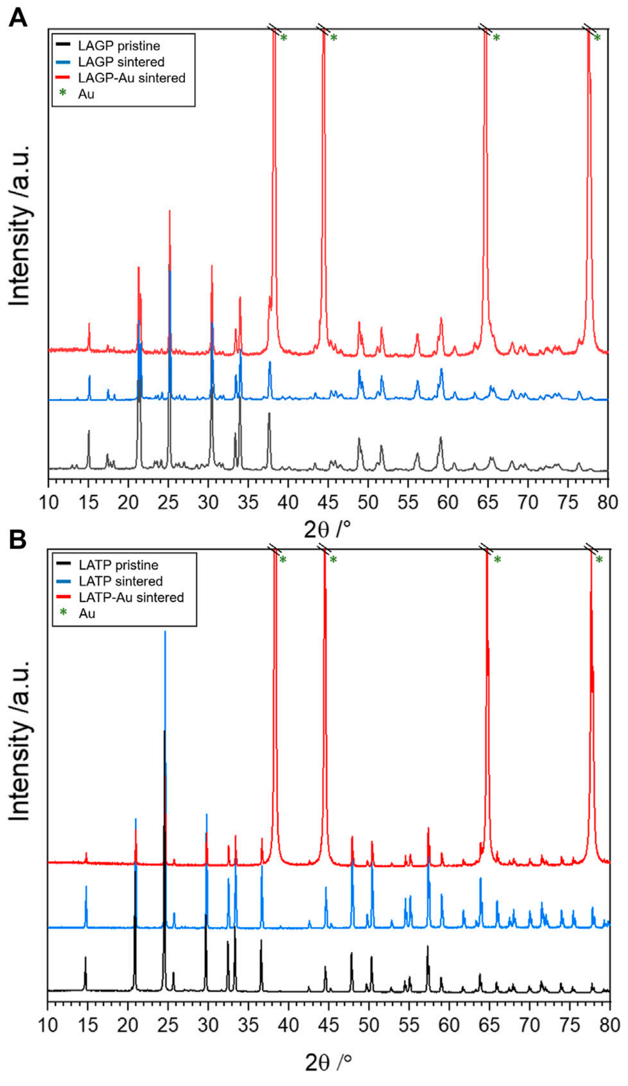

FIGURE 1 | PXRD pattern of **(A)** LAGP and **(B)** LATP pristine powders compared to the sintered pellets, with and without gold particles, using SPS.

Figure 1 displays the PXRD patterns of the pristine materials used in the present study, after sintering the solid electrolyte pellets and after sintering the composite electrodes. In **Figure 1A**, the PXRD pattern of the sintered LAGP pellet overlaps perfectly with the pattern of the pristine material (non-sintered) and corresponds to the NASICON-type structure crystallizing in the R-3c space group. No other peak is visible on the pattern confirming that, based on PXRD analyses, no impurity is present, and no side reaction occurred after the sintering of LAGP. The sintered stack was also analyzed, the pattern of the SE-Au side is presented in the figure. It matches exactly that of the sintered LAGP except for four peaks ascribed to Au (at 38.26°, 44.46°, 64.64°, and 77.62° for Au crystallized in a cubic Fm-3m space group). This indicates that no reaction between LAGP and gold particles has occurred during sintering. No peak shift is neither detected, meaning that no elemental interdiffusion occurred at the interface between LAGP and Au. In **Figure 1B**, the patterns of pristine LATP powder, sintered LATP pellet and sintered LATP-Au composite are presented. As observed for LAGP, the PXRD pattern of the sintered LATP pellet coincides perfectly with the pattern of the pristine LATP powder. It presents only peaks expected from the R-3c space group. The peaks observed on the pattern of the LATP-Au composite electrode fit with that of the sintered LATP and Au structures. The presence of a smooth baseline and sharp peaks on the sintered LATP and LAGP pellets discards the possibility of forming an amorphous phase during sintering. Based on these PXRD analyses, we confirm that SPS does not affect the structural integrity of LATP nor LAGP and that gold particles do not interact with the SEs at any point of the sintering process.

The SPS technique allows the densification of ceramic pellets from 80% up to 95% compactity (measured density/theoretical density × 100). Such high densities are required to ensure grain cohesion and minimize the cell polarization during electrochemical cycling (Aboulaich et al., 2011). Grain cohesion is important to provide proper electronic conductivity in the composite and proper ionic conductivity throughout the whole system. In this regard, the electronic conductivity of our system was measured using a Keithley 2401 multimeter in "in plane 4-points" measuring mode. It was found to be around 5 S/cm for the SE-Au composite, proving that the sintering of gold particles successfully formed an electronic network in the composite. The complete SE-Au/SE stack was insulating (infinite resistance), proving that the sintering did not affect the insulating properties of the solid electrolyte. After sintering, the resulting pellet is shown in **Figure 2A**. It consists of a bilayered pellet with a clear separation line, visible all around the pellet's circumference, between the electrolyte (white) and the composite (golden) parts. To observe the SE-Au/SE interface in more details, the stack was polished in its cross-section and ran through SEM. A large scale view of the cross section is displayed in **Figure 2B** where both layers of the stacks are still visible and appear clean and homogeneous across several millimeters. The electrolyte side appears less bright due to its electronic insulating character. In contrast, the composite is bright all over the area owing to the electronic conduction of the gold particles. In **Figure 2C**, higher magnifications are used and allow us to determine the thickness of each part of the bilayer. Thicknesses of 200 and 400 µm were measured for SE-Au and SE sections respectively for this sample. All the sintered pellets displayed roughly the same dimensions, although the SE layer of some samples was further polished to a thickness of 150 µm before undergoing electrochemical tests. Moreover, very low internal porosity is observed on the micrographs indicating that the stack is sufficiently dense. EDS analyses were run with a highlight on Ge and Au elemental distributions over the surface of the SE-Au/SE interface. It shows a homogeneous distribution of Au in the SE-Au composite. For the sake of conciseness, only micrographs of LAGP-Au/LAGP stacks were shown, but the exact same construction is observed for LATP-Au/LATP stacks**.**

SPS allows the sintering of SE-Au and SE pellets into one compact stack while avoiding any side reaction between the SE and Au components. This confirms the suitability of SPS for producing optimal ceramic stacks for the determination of solid electrolytes ESWs. The specific surface area of the gold powder was

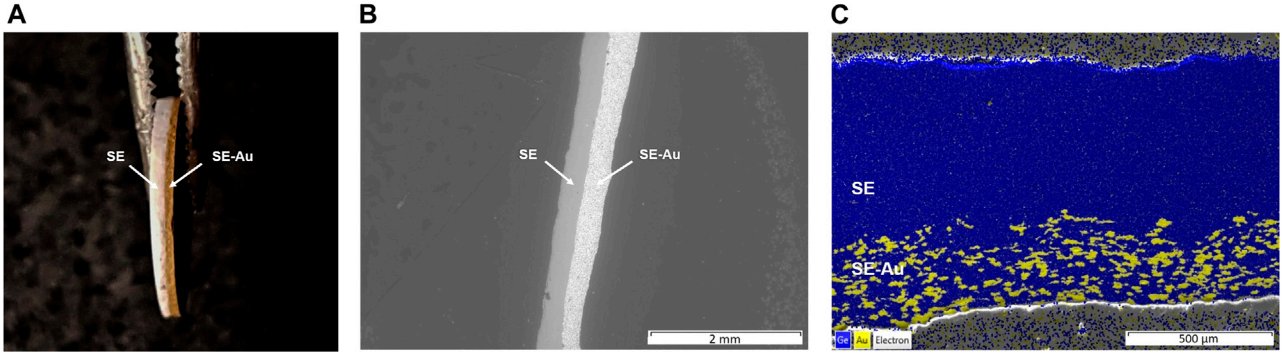

FIGURE 2 | (A) Picture of a SE-Au/SE stack after completing sintering, calcination and polishing processes, **(B)** SEM micrograph of an LAGP-Au/LAGP stack cross section (×30), gold particles appear in light gray, **(C)** SEM micrograph and corresponding EDS analysis map of an LAGP-Au/LAGP stack cross section (×120), Au is represented in yellow, Ge in blue.

measured using BET, it was estimated to be 0.4165 m^2/g. The sintered SE-Au pellets contain 100 mg of gold resulting in a contact area between SE and Au largely superior to 0.5 cm^2, which is the contact surface calculated for an 8 mm diameter SE pellet covered by an Au layer. Sintered SE and Au composite electrodes offer more electrochemical surface than conventional Au-coating on SE pellets, ensuring greater decomposition currents.

Electrochemical Measurements

To determine the electrochemical stability windows, LAGP-Au/LAGP and LATP-Au/LATP Swagelok cells were assembled. Two cells of each were used for the study of the oxidation and reduction separately. The cells were cycled using PITT, a widely used method in electrochemistry that allows the system to remain close to the thermodynamic equilibrium and to neglect interfacial resistances. This method is also used, along with galvanostatic intermittent titration technique (GITT), for determining the diffusion coefficient in electrochemical materials, such as lithium diffusion in lithium-ion battery electrodes (Wen et al., 1979). In the context of this study, PITT is used to observe the current response at each potential step after the system returns to equilibrium. Using PITT allows the observation of the first redox currents generated by LAGP and LATP, which provides us with a precise ESW. The same approach was recently used by Zhang et al. (2021) to determine the electrochemical stability of single-ion conducting polymer electrolytes. The experiment starts by recording the E_{oc} of the battery. A potential increment of 50 mV is applied for oxidation and reduction respectively. During oxidation and reduction, the SE-Au layer acts as a positive electrode and POE protected lithium metal as negative electrode. PITT curves for LAGP are given in **Figure 3**. The graph is presented as a current response vs. potential for the ease of reading, however the typical PITT response i.e. I vs. t, is displayed in **Supplementary Figure S1**. Observing the reduction curve, each potential step from the E_{oc} at *ca.* 3.0 to 1.85 V vs. Li^+/Li is followed by a small current jump that rapidly decreases to 0. Below 1.85 V, the current response increases drastically after every potential step. This current response is the signature of a possible conversion reaction of LAGP into Ge + $Li_4P_2O_7$ + $AlPO_4$ + GeO_2 initiated at this potential, as suggested by our first-principles calculations. When further decreasing the potential, another reaction starts at 1.05 V vs. Li^+/Li associated with the formation of Li_xGe alloy. This is in agreement with the experimental value reported by Zhang et al. (2017). Upon oxidation, the current response remains small and steady from 3.0 to 4.9 V vs. Li^+/Li. Above this point, a drastic increase of the current response is observed from 4.9 to 5.3 V and another increase occurs starting at 5.7 V up to above 6 V vs. Li^+/Li.

Similarly, the electrochemical stability window for LATP is presented in **Figure 4** (i.e. I vs. t, is displayed in **Supplementary Figure S2**). A noticeable reduction current is observed as early as 2.65 V and becomes more significant at 2.5 V vs. Li^+/Li. The latter value corresponds to the operating potential of $LiTi_2(PO_4)_3$ active material (Delmas et al., 1988). Upon oxidation, a noticeable oxidation current appears at 4.6 V vs. Li^+/Li. It is crucial to set the oxidation and reduction potentials for solid electrolytes at the appearance of any noticeable current response, albeit small, because they mark the presence of irreversible reactions within SEs that can lead to significant capacity loss over time. In this regard, we estimate the electrochemical stability windows to be [2.65–4.6 V] vs. Li^+/Li for LATP and [1.85–4.9 V] vs. Li^+/Li for LAGP. These ESWs, assessed using PITT, are much narrower than any value presented in **Table 1**. Regarding the oxidation potential, all the values reported resulting from CV measurements are above 5.5 V vs. Li^+/Li. Reduction potentials found in the literature are very divergent from a study to another. For LAGP, the values for the reduction potential presented are all below 1.5 V vs. Li^+/Li. It is significantly lower than the value of 1.85 V vs. Li^+/Li presented in this study. Regarding LATP, the studies found in the literature using galvanostatic cycling define the reduction potential of LATP to be the reduction potential of the Ti^{4+}/Ti^{3+} couple, around 2.5 V vs. Li^+/Li. However, the PITT curve reveals that a small LATP current response is present before that value. It is worth mentioning that PITT measurements were run at 60°C in the present study, as opposed to room temperature

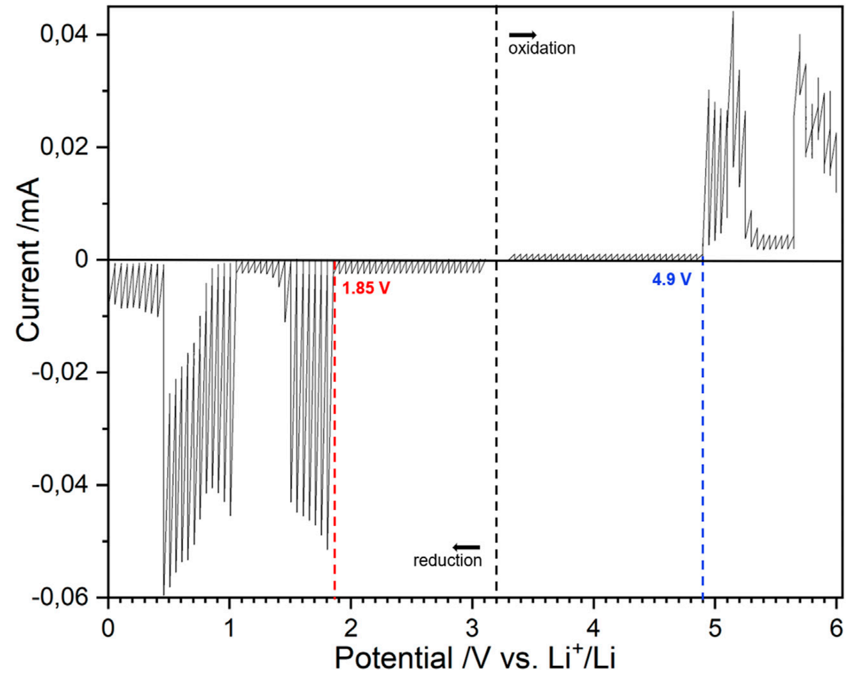

FIGURE 3 | PITT measurements on a stack LAGP-Au/LAGP represented using the current response as a function of potential. The two measures were taken on two distinct stacks at 60°C, from E_{oc} to 6 V for oxidation and from E_{oc} to 0 V vs. Li^+/Li for reduction. A potential step of 50 mV, a current limit of 10 nA and a time limit of 3 h were used.

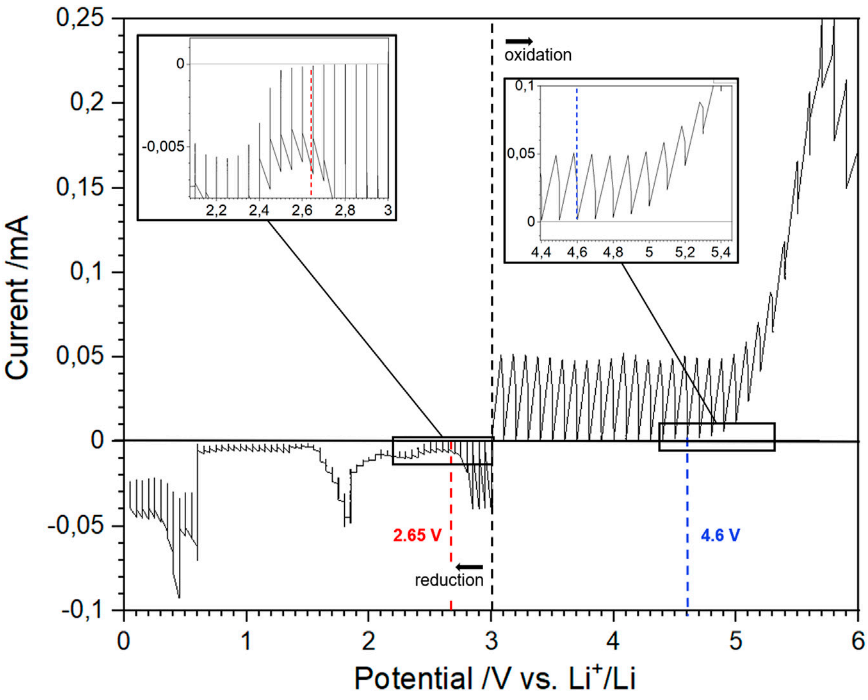

FIGURE 4 | PITT measurements on a stack LATP-Au/LATP. The two measures were taken on two distinct stacks at 60°C, from E_{oc} to 6 V for oxidation and from E_{oc} to 0 V vs. Li^+/Li for reduction. A potential step of 50 mV, a current limit of 10 nA and a time limit of 3 h were used.

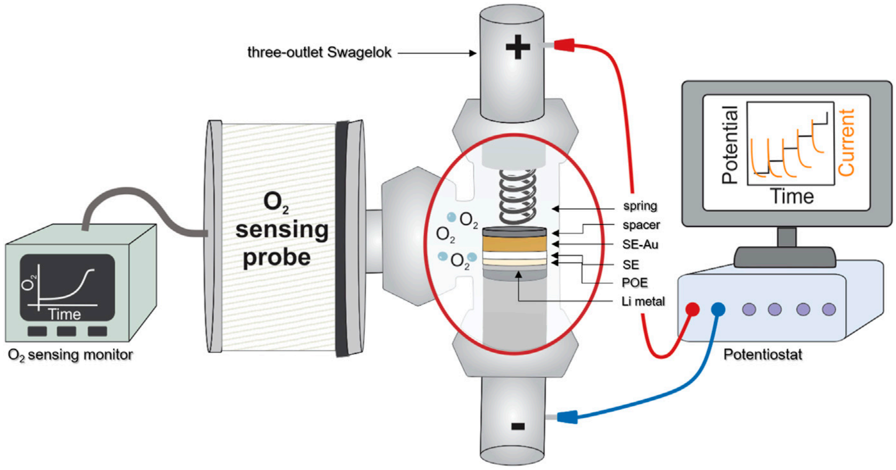

FIGURE 5 | Schematic representation of the setup combining O_2 sensing and PITT measurements.

which, by compliance to Nernst law, has a direct influence on the potential. However, temperature differences of this order are expected to only alter the ESW in a negligible way.

O_2 Sensing Measurements

Decomposition products upon reduction, especially against lithium metal, were widely investigated for LAGP (Paolella et al., 2020; Sun et al., 2020) and LATP (Hartmann et al., 2013; Chung and Kang, 2017; Inozemtseva et al., 2020; Zhu et al., 2020; Hou et al., 2020). However, experimental studies on their decomposition upon oxidation are nonexistent. First-principles calculations have been used to foresee these products but to the best of our knowledge, no experimental study has been successful yet in the determination of such decomposition products at high potential. O_2 being among the decomposition products predicted by first-principles calculations (**Table 2**), we used an oxygen sensing probe to investigate the possibility of O_2 production at LATP and LAGP oxidation potentials. The setup is presented in **Figure 5**, the electrochemical cell is coupled to the sensing probe so that the amount of O_2 produced is detected *operando*. Results of this experiment are shared in **Figure 6**. The objective of this experiment was to correlate the amount of charge going through the system with the amount of O_2 released, as expected from our calculations. Accelerated PITT was used to avoid diluting the O_2 signal in extended relaxation times. Done this way, it is possible to observe a sharper signal for O_2 generated as a function of time. The ESW might be slightly altered by this change of parameters but the experiment is focused primarily on detecting a clear evolution of O_2 upon oxidation. For both LAGP and LATP, the amount of O_2 detected follows a smooth baseline during the relaxation period (left at E_{oc} for 6 h) and during the beginning of the accelerated PITT, confirming that no O_2-producing reaction is occurring in this potential range, When the oxidation potentials are reached at 4.9 and 4.6 V vs. Li^+/Li for LAGP (**Figure 6A**) and LATP (**Figure 6B**) respectively, we observe a slow increase of the amount of O_2 at start, followed by a rapid increase when the potential and charge increase. The curve representing the charge as a function of time is in perfect overlap with the evolution of O_2, showing the direct relation between the generated electric charges and the production of O_2. This first observation validates that O_2 is a decomposition product of LATP and LAGP, as predicted by first-principles calculations. It is worth mentioning that, although LAGP and LATP were introduced in the same quantities (≈40 mg), the electric charge from the degradation of LATP is 10× that of LAGP. Due to the lack of control over the initial amount of O_2 present in the cell, it was only possible to present qualitative results of O_2 production. An optimization of the setup is currently considered to traceback the quantitative amount of O_2 released from LATP and LAGP oxidations.

Using PXRD, a first attempt to characterize the decomposition products predicted by our computations failed to show the presence of crystalline phases such as $AlPO_4$, $Ge_5O(PO_4)_6$, TiP_2O_7, and $LiPO_3$ after LAGP or LATP oxidations. Our hypotheses are that the decomposition products are 1) amorphous and/or 2) present in very small amount due the solid character of our compounds. Indeed, only the grains of SE that are directly in contact with gold particles get to react. The effective potential vehicled by the gold particles reaches this first layer of SE. However, assuming that the SE particles and their decomposition products are electronic insulators, the second layer of SE grains will not be affected by the potential applied on the gold particles. This system impedes the effective potential to reach the rest of the SE layers which are, therefore, not oxidized.

Transmission Electron Microscopy

TEM observations were carried out to investigate the oxidation reaction of LAGP within the LAGP-Au composite before and after cycling. The micrograph presented in **Figure 7A** displays a sintered LAGP-Au thin lamella. The conductive gold particles (in black) are surrounded by LAGP ceramic grains (in gray). It was possible to measure the size of LAGP particles, they lie between 500 and 800 nm (**Supplementary Figure S3A**). Selected area electron diffraction (SAED) measurements confirmed the crystalline nature of Au

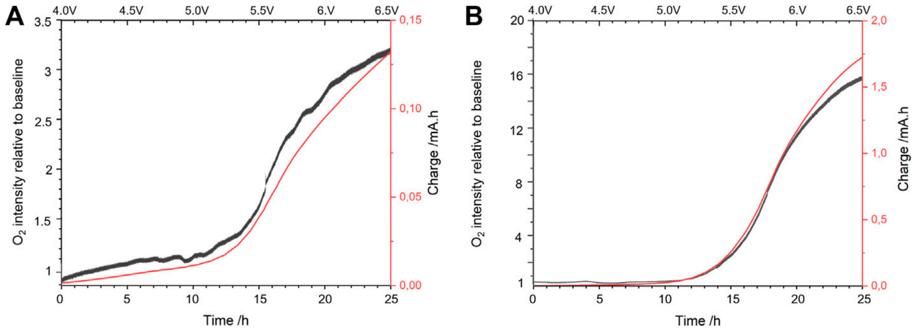

FIGURE 6 | *Operando* O_2 sensing measurements for **(A)** LAGP and **(B)** LATP coupled to accelerated PITT in oxidation. SE-Au/SE stacks of LAGP and LATP were used within three-outlet Swagelok cells. The accelerated PITT is presented as the charge Q as a function of time. A potential step of 100 mV, a current limit of 10 nA and a time limit of 1 h were used.

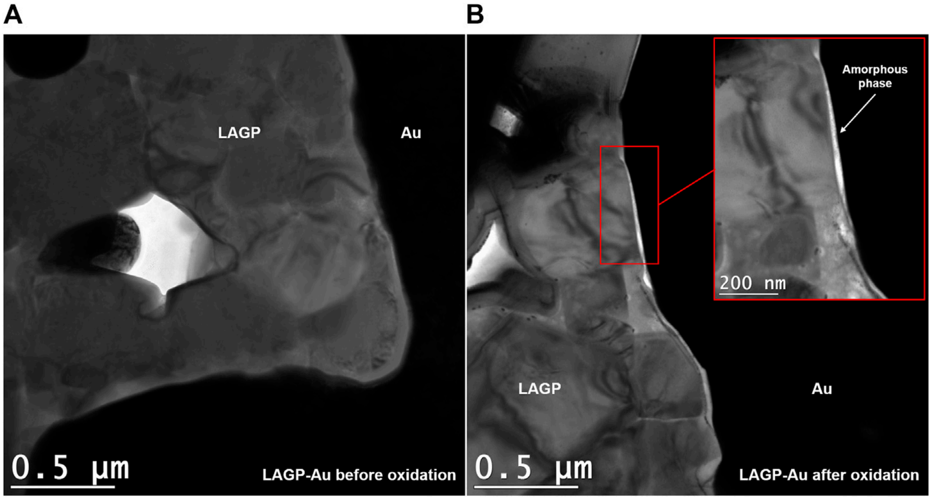

FIGURE 7 | Bright-field TEM micrographs (×10k) of two LAGP-Au composite samples **(A)** before and **(B)** after oxidation. The inset was observed at ×25k.

and LAGP particles. The selected patterns show interplanar spacings of 2.36 Å for Au-(111) (Dilshad et al., 2012) and 3.66 Å for LAGP-(113) (Wang et al., 2020) (**Supplementary Figures S4A,B**). Very few cavities are observed between the grains (except the ones created by the ion beam), confirming the good sintering of the particles. Micrographs collected for the LAGP-Au composite after oxidation are displayed in **Figure 7B**. The same distribution is observed for LAGP grains with sizes ranging from 500 to 800 nm. A layer is observed at the LAGP-Au interface with a thickness ranging from 10 to 30 nm (**Supplementary Figures S3B–D**), the bright white color seen on the TEM micrograph and the continuous circle observed from SAED measurements point out to an amorphous phase (**Supplementary Figure S4C**). Information collected through TEM and SAED measurements indicate that the LAGP layer in contact with Au underwent a phase transformation leading to the formation of amorphous decomposition products, possibly $Ge_5O(PO_4)_6$, $AlPO_4$, and $LiPO_3$ predicted by first-principles calculations, but which is difficult to confirm experimentally at this stage.

EIS measurements were carried out from E_{oc} to 5.6 V and are presented in **Supplementary Figure S5**. The first semi-circle observed at high frequencies (7 kHz) is attributed to the bulk SE and remains constant, independently of the applied potential. At lower frequencies, we observe a tail, which is attributed to the charge accumulation at the Au blocking electrode from E_{oc} to 4.9 V. Passed this potential, another large semi-circle (i.e. associated resistance above 4 MΩ) appears, which confirms that a sluggish charge transfer process now occurs at the SE-Au interface above 4.9 V vs. Li^+/Li. This is in agreement with the PITT measurement showing that a faradaic reaction starts above this potential.

CONCLUSION

The experimental setup used in this study enabled the determination of accurate ESWs for LAGP and LATP solid electrolytes with carefully selected parameters: using inert gold particles instead of carbon black singled out the redox mechanisms of the solid electrolytes, sintering SEs with gold particles into composites enhanced the redox current responses and using PITT allowed to work close to the thermodynamic equilibrium of the system. The electrochemical stability windows were found to be [1.85–4.9 V] vs. Li^+/Li for LAGP and [2.65–4.6 V] vs. Li^+/Li for LATP. An oxygen sensing probe coupled to the PITT was used to observe *operando* the decomposition of LAGP and LATP upon oxidation to produce O_2, as predicted by first-principles calculations. The presence of an amorphous phase at the SE-Au interface after cycling was observed through TEM measurements. EIS results indicate that the amorphous phase might be insulating. The values reported in the present manuscript are much narrower than commonly admitted in the community. An accurate determination of the SEs' ESWs and their decomposition processes is crucial to the successful development of ASSLBs with prolonged cycle life and high coulombic efficiency. The experimental setup coupling PITT and *operando* O_2 sensing put in place herein is accessible to all, it will be the object of further optimization to allow a precise quantification of O_2. It is believed to enable many other studies involving the release of O_2. Assessing the ESW of other solid electrolytes; ceramic, polymer and/or composites, is currently investigated and will be the subject of future publications.

DATA AVAILABILITY STATEMENT

The original contributions presented in the study are included in the article/**Supplementary Material**, further inquiries can be directed to the corresponding author.

AUTHOR CONTRIBUTIONS

YB, SR, and MD conceived the project. YB carried out the experiments, performed the computations and wrote the manuscript with support from SR. MR carried out the syntheses. GH supervised the computational part. MD supervised the experimental part. GH and MD reviewed the article and provided funding for the present study.

FUNDING

YB is grateful for the financial support of the Fonds de la Recherche Scientifique – FNRS of Belgium through a FRIA grant (FC31481) and the Natural Sciences and Engineering Research Council of Canada - NSERC through a BESC D grant (BESCD3-534841-2019). MR, SR, and MD acknowledge the financial support received from the Natural Sciences and Engineering Research Council of Canada (NSERC RDCPJ 528052-18).

ACKNOWLEDGMENTS

We thank D. Lepage for his valuable insight into the experimental part, G. Bokas and S. Posada-Pérez for their help on the computational section. We acknowledge the contribution of J.-P. Masse to the analysis and interpretation of the TEM results. The present research benefited from computational resources provided by the Université catholique de Louvain (CISM/UCLouvain) and by the Consortium des Équipements de Calcul Intensif en Fédération Wallonie-Bruxelles (CÉCI).

SUPPLEMENTARY MATERIAL

The Supplementary Material for this article can be found online at: https://www.frontiersin.org/articles/10.3389/fenrg.2021.682008/full#supplementary-material

REFERENCES

Aboulaich, A., Bouchet, R., Delaizir, G., Seznec, V., Tortet, L., Morcrette, M., et al. (2011). A New Approach to Develop Safe All-Inorganic Monolithic Li-Ion Batteries. *Adv. Energ. Mater.* 1 (2), 179–183. doi:10.1002/aenm.201000050

Alpen, U. v., Bell, M. F., Wichelhaus, W., Cheung, K. Y., and Dudley, G. J. (1978). Ionic Conductivity of Li14Zn(GeO44 (Lisicon). *Electrochimica Acta* 23 (12), 1395–1397. doi:10.1016/0013-4686(78)80023-1

Aurbach, D., Zinigrad, E., Cohen, Y., and Teller, H. (2002). A Short Review of Failure Mechanisms of Lithium Metal and Lithiated Graphite Anodes in Liquid Electrolyte Solutions. *Solid State Ionics* 148 (3), 405–416. doi:10.1016/S0167-2738(02)00080-2

Auvergniot, J., Cassel, A., Ledeuil, J.-B., Viallet, V., Seznec, V., and Dedryvère, R. (2017). Interface Stability of Argyrodite Li6PS5Cl toward LiCoO2, LiNi1/3Co1/3Mn1/3O2, and LiMn2O4 in Bulk All-Solid-State Batteries. *Chem. Mater.* 29 (9), 3883–3890. doi:10.1021/acs.chemmater.6b04990

Bag, S., and Thangadurai, V. (2020). CHAPTER 3 Electrolyte Development for Solid-State Lithium Batteries. In *Energy Storage and Conversion Materials*. London, UK: The Royal Society of Chemistry, 100–135.

Bard, A. J., and Faulkner, L. R. (2000). *Electrochemical Methods and Applications*. New York; London: Wiley-Interscience.

Birke, P., Salam, F., Döring, S., and Weppner, W. (1999). A First Approach to a Monolithic All Solid State Inorganic Lithium Battery. *Solid State Ionics* 118 (1), 149–157. doi:10.1016/S0167-2738(98)00462-7

Blöchl, P. E. (1994). Projector Augmented-Wave Method. *Phys. Rev. B* 50 (24), 17953–17979. doi:10.1103/PhysRevB.50.17953

Chen, S., Xie, D., Liu, G., Mwizerwa, J. P., Zhang, Q., Zhao, Y., et al. (2018). Sulfide Solid Electrolytes for All-Solid-State Lithium Batteries: Structure, Conductivity, Stability and Application. *Energ. Storage Mater.* 14, 58–74. doi:10.1016/j.ensm.2018.02.020

Chung, H., and Kang, B. (2017). Mechanical and Thermal Failure Induced by Contact between a Li1.5Al0.5Ge1.5(PO4)3 Solid Electrolyte and Li Metal in an All Solid-State Li Cell. *Chem. Mater.* 29 (20), 8611–8619. doi:10.1021/acs.chemmater.7b02301

Cui, Y., Rohde, M., Reichmann, T. L., Mahmoud, M. M., Ziebert, C., and Seifert, H. J. (2016). Ionic Conductivity and Stability of the Lithium Aluminum Germanium Phosphate. *ECS Trans.* 72 (8), 139–146. doi:10.1149/07208.0139ecst

Delaizir, G., Viallet, V., Aboulaich, A., Bouchet, R., Tortet, L., Seznec, V., et al. (2012). The Stone Age Revisited: Building a Monolithic Inorganic Lithium-Ion Battery. *Adv. Funct. Mater.* 22 (10), 2140–2147. doi:10.1002/adfm.201102479

Delmas, C., Nadiri, A., and Soubeyroux, J. L. (1988). The Nasicon-type Titanium Phosphates Ati2(PO4)3 (A=Li, Na) as Electrode Materials. *Solid State Ionics* 28-30, 419–423. doi:10.1016/S0167-2738(88)80075-4

Dewey, C. S., Lefforge, P. K., and Cabot, G. L. (1932). Moisture Sorption by Carbon Black. *Ind. Eng. Chem.* 24 (9), 1045–1050. doi:10.1021/ie50273a019

Dilshad, N., Ansari, M. S., Beamson, G., and Schiffrin, D. J. (2012). Amines as Dual Function Ligands in the Two-phase Synthesis of Stable AuxCu(1−x) Binary Nanoalloys. *J. Mater. Chem.* 22 (21), 10514–10524. doi:10.1039/C2JM31709E

Feng, J. K., Lu, L., and Lai, M. O. (2010). Lithium Storage Capability of Lithium Ion Conductor Li1.5Al 0.5Ge1.5(PO4)3.

Feng, J. K., Yan, B. G., Liu, J. C., Lai, M. O., and Li, L. (2013). All Solid State Lithium Ion Rechargeable Batteries Using NASICON Structured Electrolyte. *Mater. Technol.* 28 (5), 276–279. doi:10.1179/1753555713Y.0000000085

Foran, G., Mankovsky, D., Verdier, N., Lepage, D., Prébé, A., Aymé-Perrot, D., et al. (2020). The Impact of Absorbed Solvent on the Performance of Solid Polymer Electrolytes for Use in Solid-State Lithium Batteries. *iScience* 23 (10), 101597. doi:10.1016/j.isci.2020.101597

Fu, J. (1997). Fast Li+ Ion Conduction in Li2O-Al2O3-TiO2-SiO2-P2o2 Glass-Ceramics. *J. Am. Ceram. Soc.* 80 (7), 1901–1903. doi:10.1111/j.1151-2916.1997.tb03070.x

Gao, Z., Sun, H., Fu, L., Ye, F., Zhang, Y., Luo, W., et al. (2018). Promises, Challenges, and Recent Progress of Inorganic Solid-State Electrolytes for All-Solid-State Lithium Batteries. *Adv. Mater.* 30 (17), 1705702. doi:10.1002/adma.201705702

Han, F., Zhu, Y., He, X., Mo, Y., and Wang, C. (2016). Electrochemical Stability of Li10 GeP2 S12 and Li7 La3 Zr2 O12 Solid Electrolytes. *Adv. Energ. Mater.* 6 (8), 1501590. doi:10.1002/aenm.201501590

Hartmann, P., Leichtweiss, T., Busche, M. R., Schneider, M., Reich, M., Sann, J., et al. (2013). Degradation of NASICON-type Materials in Contact with Lithium Metal: Formation of Mixed Conducting Interphases (MCI) on Solid Electrolytes. *J. Phys. Chem. C* 117 (41), 21064–21074. doi:10.1021/jp4051275

Hasegawa, S., Imanishi, N., Zhang, T., Xie, J., Hirano, A., Takeda, Y., et al. (2009). Study on Lithium/air Secondary Batteries-Stability of NASICON-type Lithium Ion Conducting Glass-Ceramics with Water. *J. Power Sourc.* 189 (1), 371–377. doi:10.1016/j.jpowsour.2008.08.009

Hou, M., Liang, F., Chen, K., Dai, Y., and Xue, D. (2020). Challenges and Perspectives of NASICON-type Solid Electrolytes for All-Solid-State Lithium Batteries. *Nanotechnology* 31 (13), 132003. doi:10.1088/1361-6528/ab5be7

Hupfer, T., Bucharsky, E. C., Schell, K. G., Senyshyn, A., Monchak, M., Hoffmann, M. J., et al. (2016). Evolution of Microstructure and its Relation to Ionic Conductivity in Li1+xAlxTi2−x(PO4)3. *Solid State Ionics* 288, 235–239. doi:10.1016/j.ssi.2016.01.036

Imanishi, N., Hasegawa, S., Zhang, T., Hirano, A., Takeda, Y., and Yamamoto, O. (2008). Lithium Anode for Lithium-Air Secondary Batteries. *J. Power Sourc.* 185 (2), 1392–1397. doi:10.1016/j.jpowsour.2008.07.080

Inozemtseva, A. I., Vizgalov, V. A., Kapitanova, O. O., Panin, G., Velasco Vélez, J. J., Itkis, D. M., et al. (2020). *In Situ* XPS Studies of Solid Electrolyte Electroreduction through Graphene Electrode. *J. Electrochem. Soc.* 167 (11), 110533. doi:10.1149/1945-7111/aba370

Jain, A., Ong, S. P., Hautier, G., Chen, W., Richards, W. D., Dacek, S., et al. (2013). Commentary: The Materials Project: A Materials Genome Approach to Accelerating Materials Innovation. *APL Mater.* 1 (1), 011002. doi:10.1063/1.4812323

Jiang, P., Porsgaard, S., Borondics, F., Köber, M., Caballero, A., Bluhm, H., et al. (2010). Room-Temperature Reaction of Oxygen with Gold: An *In situ* Ambient-Pressure X-Ray Photoelectron Spectroscopy Investigation. *J. Am. Chem. Soc.* 132 (9), 2858–2859. doi:10.1021/ja909987j

Kamaya, N., Homma, K., Yamakawa, Y., Hirayama, M., Kanno, R., Yonemura, M., et al. (2011). A Lithium Superionic Conductor. *Nat. Mater* 10 (9), 682–686. doi:10.1038/nmat3066

Knauth, P. (2009). Inorganic Solid Li Ion Conductors: An Overview. *Solid State Ionics* 180 (14), 911–916. doi:10.1016/j.ssi.2009.03.022

Kotobuki, M., Hoshina, K., and Kanamura, K. (2011). Electrochemical Properties of Thin TiO2 Electrode on Li1+xAlxGe2−x(PO4)3 Solid Electrolyte. *Solid State Ionics* 198 (1), 22–25. doi:10.1016/j.ssi.2011.07.003

Kresse, G., and Furthmüller, J. (1996). Efficient Iterative Schemes Forab Initiototal-Energy Calculations Using a Plane-Wave Basis Set. *Phys. Rev. B* 54 (16), 11169–11186. doi:10.1103/PhysRevB.54.11169

Lau, J., DeBlock, R. H., Butts, D. M., Ashby, D. S., Choi, C. S., and Dunn, B. S. (2018). Sulfide Solid Electrolytes for Lithium Battery Applications. *Adv. Energ. Mater.* 8 (27), 1800933. doi:10.1002/aenm.201800933

Li, W. (1997). Morphology Effects on the Electrochemical Performance of LiNi[sub 1−x]Co[sub x]O[sub 2]. *J. Electrochem. Soc.* 144 (8), 2773. doi:10.1149/1.1837894

Liang, X., Han, D., Wang, Y., Lan, L., and Mao, J. (2018). Preparation and Performance Study of a PVDF-LATP Ceramic Composite Polymer Electrolyte Membrane for Solid-State Batteries. *RSC Adv.* 8 (71), 40498–40504. doi:10.1039/C8RA08436J

Lin, D., Liu, Y., and Cui, Y. (2017). Reviving the Lithium Metal Anode for High-Energy Batteries. *Nat. Nanotech* 12 (3), 194–206. doi:10.1038/nnano.2017.16

Liu, L., Tan, S., Horikawa, T., Do, D. D., Nicholson, D., and Liu, J. (2017). Water Adsorption on Carbon - A Review. *Adv. Colloid Interf. Sci.* 250, 64–78. doi:10.1016/j.cis.2017.10.002

Liu, Z., Yu, A., and Lee, J. Y. (1999). Synthesis and Characterization of LiNi1−x−yCoxMnyO2 as the Cathode Materials of Secondary Lithium Batteries. *J. Power Sourc.* 81-82, 416–419. doi:10.1016/S0378-7753(99)00221-9

Mankovsky, D., Lepage, D., Lachal, M., Caradant, L., Aymé-Perrot, D., and Dollé, M. (2020). Water Content in Solid Polymer Electrolytes: the Lost Knowledge. *Chem. Commun.* 56 (70), 10167–10170. doi:10.1039/D0CC03556D

Meesala, Y., Jena, A., Chang, H., and Liu, R.-S. (2017). Recent Advancements in Li-Ion Conductors for All-Solid-State Li-Ion Batteries. *ACS Energ. Lett.* 2 (12), 2734–2751. doi:10.1021/acsenergylett.7b00849

Holzapfel, G. W., Nuspl, G., and Busl, S. (2012). Phase-Pure Lithium Aluminium Titanium Phosphate And Method For Its Production And Use.

Muramatsu, H., Hayashi, A., Ohtomo, T., Hama, S., and Tatsumisago, M. (2011). Structural Change of Li2S-P2s5 Sulfide Solid Electrolytes in the Atmosphere. *Solid State Ionics* 182 (1), 116–119. doi:10.1016/j.ssi.2010.10.013

Ong, S. P., Mo, Y., Richards, W. D., Miara, L., Lee, H. S., and Ceder, G. (2013). Phase Stability, Electrochemical Stability and Ionic Conductivity of the Li10±1MP2X12(M = Ge, Si, Sn, Al or P, and X = O, S or Se) Family of Superionic Conductors. *Energy Environ. Sci.* 6 (1), 148–156. doi:10.1039/C2EE23355J

Ong, S. P., Richards, W. D., Jain, A., Hautier, G., Kocher, M., Cholia, S., et al. (2013). Python Materials Genomics (Pymatgen): A Robust, Open-Source python Library for Materials Analysis. *Comput. Mater. Sci.* 68, 314–319. doi:10.1016/j.commatsci.2012.10.028

Ong, S. P., Wang, L., Kang, B., and Ceder, G. (2008). Li−Fe−P−O2 Phase Diagram from First Principles Calculations. *Chem. Mater.* 20 (5), 1798–1807. doi:10.1021/cm702327g

Orsini, F., Du Pasquier, A., Beaudoin, B., Tarascon, J. M., Trentin, M., Langenhuizen, N., et al. (1998). *In situ* Scanning Electron Microscopy (SEM) Observation of Interfaces within Plastic Lithium Batteries. *J. Power Sourc.* 76 (1), 19–29. doi:10.1016/S0378-7753(98)00128-1

Paolella, A., Zhu, W., Xu, G. L., La Monaca, A., Savoie, S., Girard, G., et al. (2020). Understanding the Reactivity of a Thin Li 1.5 Al 0.5 Ge 1.5 (PO 4) 3 Solid-State Electrolyte toward Metallic Lithium Anode. *Adv. Energ. Mater.* 10 (32), 2001497. doi:10.1002/aenm.202001497

Perdew, J. P., Burke, K., and Ernzerhof, M. (1996). Generalized Gradient Approximation Made Simple. *Phys. Rev. Lett.* 77 (18), 3865–3868. doi:10.1103/PhysRevLett.77.3865

Plummer, W. B. (1930). Moisture Content of Carbon Blacks. *Rubber Chem. Technol.* 3 (2), 185–189. doi:10.5254/1.3535472

Richards, W. D., Miara, L. J., Wang, Y., Kim, J. C., and Ceder, G. (2016). Interface Stability in Solid-State Batteries. *Chem. Mater.* 28 (1), 266–273. doi:10.1021/acs.chemmater.5b04082

Sakuda, A., Hayashi, A., and Tatsumisago, M. (2010). Interfacial Observation between LiCoO2 Electrode and Li2S−P2S5 Solid Electrolytes of All-Solid-State Lithium Secondary Batteries Using Transmission Electron Microscopy. *Chem. Mater.* 22 (3), 949–956. doi:10.1021/cm901819c

Schwietert, T. K., Arszelewska, V. A., Wang, C., Yu, C., Vasileiadis, A., de Klerk, N. J. J., et al. (2020). Clarifying the Relationship between Redox Activity and Electrochemical Stability in Solid Electrolytes. *Nat. Mater.* 19, 428–435. doi:10.1038/s41563-019-0576-0

Shi, X., Ma, N., Wu, Y., Lu, Y., Xiao, Q., Li, Z., et al. (2018). Fabrication and Electrochemical Properties of LATP/PVDF Composite Electrolytes for Rechargeable Lithium-Ion Battery. *Solid State Ionics* 325, 112–119. doi:10.1016/j.ssi.2018.08.010

Sun, Q., He, L., Zheng, F., Wang, Z., An Oh, S. J., Sun, J., et al. (2020). Decomposition Failure of Li1.5Al0.5Ge1.5(PO4)3 Solid Electrolytes Induced by Electric Field: A Multi-Scenario Study Using Scanning Probe Microscopy-Based Techniques. *J. Power Sourc.* 471, 228468. doi:10.1016/j.jpowsour.2020.228468

Thackeray, M. M., David, W. I. F., Bruce, P. G., and Goodenough, J. B. (1983). Lithium Insertion into Manganese Spinels. *Mater. Res. Bull.* 18 (4), 461–472. doi:10.1016/0025-5408(83)90138-1

Thokchom, J. S., and Kumar, B. (2008). Composite Effect in Superionically Conducting Lithium Aluminium Germanium Phosphate Based Glass-Ceramic. *J. Power Sourc.* 185 (1), 480–485. doi:10.1016/j.jpowsour.2008.07.009

Tian, Y., Shi, T., Richards, W. D., Li, J., Kim, J. C., Bo, S.-H., et al. (2017). Compatibility Issues between Electrodes and Electrolytes in Solid-State Batteries. *Energ. Environ. Sci.* 10 (5), 1150–1166. doi:10.1039/C7EE00534B

Vetter, K. J., and Berndt, D. (1958). Stromdichte- und pH-Abhängigkeit des elektrochemischen Auf- und Abbaus von Oxydschichten auf Pt, Pd und Au. *Zeitschrift für Elektrochemie. Berichte der Bunsengesellschaft für physikalische Chem.* 62 (3), 378–386. doi:10.1002/bbpc.19580620329

Wang, J., Huang, G., Yan, J.-M., Ma, J.-L., Liu, T., Shi, M.-M., et al. (2020). Hybrid Solid Electrolyte Enabled Dendrite-free Li Anodes for High-Performance Quasi-Solid-State Lithium-Oxygen Batteries. *Natl. Sci. Rev.* 8 (2). doi:10.1093/nsr/nwaa150

Weber, D. A., Senyshyn, A., Weldert, K. S., Wenzel, S., Zhang, W., Kaiser, R., et al. (2016). Structural Insights and 3D Diffusion Pathways within the Lithium Superionic Conductor Li10GeP2S12. *Chem. Mater.* 28 (16), 5905–5915. doi:10.1021/acs.chemmater.6b02424

Wen, C. J., Boukamp, B. A., Huggins, R. A., and Weppner, W. (1979). Thermodynamic and Mass Transport Properties of "LiAl". *J. Electrochem. Soc.* 126 (12), 2258–2266. doi:10.1149/1.2128939

Wenzel, S., Leichtweiss, T., Krüger, D., Sann, J., and Janek, J. (2015). Interphase Formation on Lithium Solid Electrolytes-An In Situ Approach to Study Interfacial Reactions by Photoelectron Spectroscopy. *Solid State Ionics* 278, 98–105. doi:10.1016/j.ssi.2015.06.001

Wenzel, S., Randau, S., Leichtweiß, T., Weber, D. A., Sann, J., Zeier, W. G., et al. (2016). Direct Observation of the Interfacial Instability of the Fast Ionic Conductor Li10GeP2S12 at the Lithium Metal Anode. *Chem. Mater.* 28 (7), 2400–2407. doi:10.1021/acs.chemmater.6b00610

Winter, M., and Besenhard, J. O. (1999). Wiederaufladbare Batterien. *Chem. Unserer Zeit* 33 (6), 320–332. doi:10.1002/ciuz.19990330603

Xiao, W., Wang, J., Fan, L., Zhang, J., and Li, X. (2019). Recent Advances in Li1+xAlxTi2−x(PO4)3 Solid-State Electrolyte for Safe Lithium Batteries. *Energ. Storage Mater.* 19, 379–400. doi:10.1016/j.ensm.2018.10.012

Xiao, Y., Miara, L. J., Wang, Y., and Ceder, G. (2019). Computational Screening of Cathode Coatings for Solid-State Batteries. *Joule* 3 (5), 1252–1275. doi:10.1016/j.joule.2019.02.006

Xu, X., Wen, Z., Wu, X., Yang, X., and Gu, Z. (2007). Lithium Ion-Conducting Glass? Ceramics of Li1.5Al0.5Ge1.5(PO4)3?xLi2O (x=0.0?0.20) with Good Electrical and Electrochemical Properties. *J. Am. Ceram. Soc.* 90 (9), 2802–2806. doi:10.1111/j.1551-2916.2007.01827.x

Xu, X., Wen, Z., Yang, X., Zhang, J., and Gu, Z. (2006). High Lithium Ion Conductivity Glass-Ceramics in Li2O-Al2O3-TiO2-P2o5 from Nanoscaled Glassy Powders by Mechanical Milling. *Solid State Ionics* 177 (26), 2611–2615. doi:10.1016/j.ssi.2006.04.010

Yoshio, M., Noguchi, H., Itoh, J.-i., Okada, M., and Mouri, T. (2000). Preparation and Properties of LiCoyMnxNi1−x−yO2 as a Cathode for Lithium Ion Batteries. *J. Power Sourc.* 90 (2), 176–181. doi:10.1016/S0378-7753(00)00407-9

Zhang, Q., Cao, D., Ma, Y., Natan, A., Aurora, P., and Zhu, H. (2019). Sulfide-Based Solid-State Electrolytes: Synthesis, Stability, and Potential for All-Solid-State Batteries. *Adv. Mater.* 31 (44), 1901131. doi:10.1002/adma.201901131

Zhang, W., Feng, S., Huang, M., Qiao, B., Shigenobu, K., Giordano, L., et al. (2021). Molecularly Tunable Polyanions for Single-Ion Conductors and Poly(solvate Ionic Liquids). *Chem. Mater.* 33 (2), 524–534. doi:10.1021/acs.chemmater.0c03258

Zhang, Z., Shao, Y., Lotsch, B., Hu, Y.-S., Li, H., Janek, J., et al. (2018). New Horizons for Inorganic Solid State Ion Conductors. *Energ. Environ. Sci.* 11 (8), 1945–1976. doi:10.1039/C8EE01053F

Zhang, Z., Zhang, L., Liu, Y., Yu, C., Yan, X., Xu, B., et al. (2018). Synthesis and Characterization of Argyrodite Solid Electrolytes for All-Solid-State Li-Ion Batteries. *J. Alloys Compd.* 747, 227–235. doi:10.1016/j.jallcom.2018.03.027

Zhang, Z., Zhao, Y., Chen, S., Xie, D., Yao, X., Cui, P., et al. (2017). An Advanced Construction Strategy of All-Solid-State Lithium Batteries with Excellent Interfacial Compatibility and Ultralong Cycle Life. *J. Mater. Chem. A.* 5 (32), 16984–16993. doi:10.1039/C7TA04320A

Zheng, F., Kotobuki, M., Song, S., Lai, M. O., and Lu, L. (2018). Review on Solid Electrolytes for All-Solid-State Lithium-Ion Batteries. *J. Power Sourc.* 389, 198–213. doi:10.1016/j.jpowsour.2018.04.022

Zhu, J., Zhao, J., Xiang, Y., Lin, M., Wang, H., Zheng, B., et al. (2020). Chemomechanical Failure Mechanism Study in NASICON-type Li1.3Al0.3Ti1.7(PO4)3 Solid-State Lithium Batteries. *Chem. Mater.* 32 (12), 4998–5008. doi:10.1021/acs.chemmater.9b05295

Zhu, Y., He, X., and Mo, Y. (2016). First Principles Study on Electrochemical and Chemical Stability of Solid Electrolyte-Electrode Interfaces in All-Solid-State Li-Ion Batteries. *J. Mater. Chem. A.* 4 (9), 3253–3266. doi:10.1039/C5TA08574H

Zhu, Y., He, X., and Mo, Y. (2015). Origin of Outstanding Stability in the Lithium Solid Electrolyte Materials: Insights from Thermodynamic Analyses Based on First-Principles Calculations. *ACS Appl. Mater. Inter.* 7 (42), 23685–23693. doi:10.1021/acsami.5b07517

Conflict of Interest: The authors declare that the research was conducted in the absence of any commercial or financial relationships that could be construed as a potential conflict of interest.